

Surface wave tomography of the upper mantle beneath the Reykjanes Ridge with implications for ridge–hot spot interaction

Andrew A. Delorey,^{1,2} Robert A. Dunn,¹ and James B. Gaherty³

Received 4 October 2006; revised 20 April 2007; accepted 1 May 2007; published 24 August 2007.

[1] We modeled fundamental mode Love and Rayleigh waves to study the seismic properties of the upper mantle beneath the Reykjanes Ridge. These waves were generated by regional earthquakes occurring in the North Atlantic to the south of Iceland and were recorded by stations located on Iceland. Over 12,000 measurements of the phase, group arrival time, and amplitude of narrow-pass-filtered waveforms (over the period range of 9.5–100 s) were used to solve for mantle shear wave velocity structure and anisotropy. In a vertical plane oriented normal to the ridge axis, the velocity structure contains a broad and deep low-velocity zone in the upper mantle beneath the ridge. A joint analysis of the seismic structure with gravity data reveals that the low velocities are consistent with elevated temperatures ($\sim 75^\circ$). Our study shows that plume material spreads broadly outward beneath the Reykjanes Ridge from Iceland and is not confined to a narrow lithospheric channel. At distances >200 km from the ridge, shear wave anisotropy indicates a predominant horizontal alignment of the fast axes of anisotropic crystals (mainly above 50 km depth), which can be interpreted as past, horizontal, ridge-perpendicular flow. Within ± 200 km of the ridge the anisotropy indicates a general vertical alignment of the fast axes or an alignment such that the fast axes point along the ridge. The transition to this type of anisotropy coincides with the appearance of increased hot spot–ridge interaction ~ 20 Myr ago, indicating that plume flow has largely disrupted mantle flow beneath the ridge since that time.

Citation: Delorey, A. A., R. A. Dunn, and J. B. Gaherty (2007), Surface wave tomography of the upper mantle beneath the Reykjanes Ridge with implications for ridge–hot spot interaction, *J. Geophys. Res.*, 112, B08313, doi:10.1029/2006JB004785.

1. Introduction

[2] Extensive volcanism at Iceland over the past 55+ million years [Morgan, 1981] is usually ascribed to the existence of a hot, buoyant, mantle plume [Morgan, 1971; White and McKenzie, 1989; Wolfe *et al.*, 1997; Allen *et al.*, 1999]. Likewise, along the adjacent Reykjanes and Kolbeinsey mid-ocean ridges, geochemical [e.g., Schilling, 1973; Fitton *et al.*, 1997; Murton *et al.*, 2002], seismic [e.g., Smallwood *et al.*, 1995; White *et al.*, 1995; Pilidou *et al.*, 2004], and seafloor morphological [e.g., Searle *et al.*, 1998] evidence for high mantle melt production is usually attributed to outward flow of plume material beneath these ridges. Although debate continues over the origin of these observations [Foulger and Pearson, 2001], seismic tomographic images reveal a plume-like structure in the upper mantle beneath Iceland [Wolfe *et al.*, 1997; Foulger *et al.*, 2000; Allen *et al.*, 2002; Zhao, 2004] and several plume

flow models have been developed to explain Icelandic volcanism and the observations along the adjacent ridges. While the observations are most often attributed to sublithospheric spreading of plume material away from Iceland [Vogt, 1976; Ribe *et al.*, 1995; Ito *et al.*, 1996, 1999; Albers and Christensen, 2001; Ito, 2001], the exact manner of such spreading has not been determined.

[3] At least two end-member models have been proposed to describe how a plume might spread outward beneath the Reykjanes Ridge. They are distinguished by whether the plume material is preferentially channeled down the ridge in a lithospheric channel or spreads out radially beneath the lithosphere. In the channel flow model [Albers and Christensen, 2001], lithospheric cooling generates a rheological groove beneath the ridge via thickening of the lithosphere away from the ridge. Buoyant, low-viscosity plume material, rising in a narrow conduit beneath Iceland, is trapped and channeled within this groove. In this model, low-viscosity plume material is needed to explain the lateral extent of trace element concentrations [Schilling, 1973, 1985] and large-scale topography and gravity anomalies [White, 1997]. In an alternate model, plume material spreads out in a radial manner away from Iceland [Ito *et al.*, 2003]. This may occur if the viscosity contrast between the plume material and the ambient mantle is less than 2 orders of magnitude, or if the plume layer thickness is large compared to the variation in lithospheric thickness. Radial

¹Department of Geology and Geophysics, School of Ocean and Earth Science and Technology, University of Hawaii, Honolulu, Hawaii, USA.

²Now at Earth and Space Sciences, University of Washington, Seattle, Washington, USA.

³Lamont-Doherty Earth Observatory of Columbia University, Palisades, New York, USA.

spreading may be enhanced by mantle dehydration at the onset of partial melting, which may fill the lithospheric groove with higher-viscosity dehydrated plume material [Hirth and Kohlstedt, 1996]. Since the depth of the dehydration/high-viscosity boundary does not change significantly away from the ridge axis, lower-viscosity plume material spreads out radially beneath this boundary [Ito et al., 1999; Ito, 2001].

[4] We use the multispectral finite-frequency surface wave tomography method of Dunn and Forsyth [2003] to examine the anisotropic shear wave structure of the upper mantle beneath the Reykjanes Ridge and to infer mantle flow, lithospheric thickness, thermal structure, and melt distribution in the mantle. We use the results to distinguish whether plume material flows preferentially beneath the ridge, spreads out radially, or something in between.

2. Study Area

[5] The study area encompasses the 1000 km long Reykjanes Ridge and the 400 km section of the Mid-Atlantic Ridge (MAR) between the Bight and Charlie-Gibbs fracture zones (Figure 1). This is a slow spreading ridge with full spreading rates that range from 18.5 mm/yr in the north, to 20.2 mm/yr in the south [DeMets et al., 1994]. Crustal accretion is symmetric about the ridge [Searle et al., 1998] even though the spreading direction is oblique to the strike of the ridge (28° from ridge normal). In a hot spot reference frame [Gripp and Gordon, 2002], the ridge axis currently migrates southwest at ~2 cm/yr; the North American plate migrates to the west-south-west at ~2.9 cm/yr and the Eurasian Plate migrates south-south-west at ~1.3 cm/yr.

[6] When compared to other “normal” slow spreading ridges, the Reykjanes Ridge has many anomalous characteristics that suggest southward flow of plume material beneath the ridge. Seafloor morphology, gravity, and seismic measurements of crustal thickness provide first-order evidence for increased melt generation and associated mantle temperature or composition anomalies. For example, the average ocean depth for the MAR is ~2.5 km. However, over a distance of 1350 km the axial depth of the MAR slowly rises from 2.5 km depth, just south of the Bight Fracture Zone, to sea level on the Reykjanes Peninsula [White et al., 1995]. This trend can be explained by a combination of thickening crust [Smallwood et al., 1995; Heller and Marquart, 2002] and more buoyant material in the upper mantle [Heller and Marquart, 2002]. Seismic estimates of crustal thickness indicate that the crust increases from 6–7 km thick at a distance of 1500 km from central Iceland [Whitmarsh and Calvert, 1986], to 8–12 km under the northern Reykjanes Ridge [Smallwood et al., 1995], to 38–40 km under central Iceland [Darbyshire et al., 1998]. An admittance study [Heller and Marquart, 2002] indicates that the ridge is at least partially supported by low-density material in the asthenosphere.

[7] The general lack of lithospheric segmentation, a characteristic of the Reykjanes Ridge north of the Bight Fracture Zone, and an axial high instead of an axial valley, typical of the Reykjanes Ridge north of 58°50'N, are both signatures of a high melt supply [Talwani, 1971; Keeton et al., 1997]. Reduced segmentation of the lithosphere also

coincides with the absence of large-amplitude, segment-scale, mantle Bouguer gravity anomaly variations, as seen elsewhere on the MAR, and nearly linear magnetic isochrons out to 10 Myr from the ridge [Searle et al., 1998]. V-shaped ridges are observed in both bathymetry and gravity data that flank the ridge axis and are oriented subparallel to the strike of the spreading axis [e.g., Vogt, 1976; Searle et al., 1998]. These ridges are thought to be caused by pulses of hot (+30°C) plume material that propagate down the ridge at a rate ten times faster than the half seafloor spreading rate [White et al., 1995]. Such pulses have a primary periodicity of 5–6 Myr [Vogt, 1971; Jones et al., 2002] and generate 2 km of excess crustal thickness [Vogt, 1971; White et al., 1995; Ito, 2001] and a high density of seamounts [Searle et al., 1998]. Periods of anomalously high melting beneath Iceland are correlated with, and may be the cause of, ridge jumps on Iceland [Jones et al., 2002]. Alternatively, periods of elevated magma supply may be the result, rather than the cause, of these ridge jumps [White et al., 1995; Hardarson et al., 1997]. The current mode of spreading at the Reykjanes Ridge has been active for only ~20 Ma; the previous mode has no V-shaped ridges, and there is evidence for segmented, normal (rather than oblique) spreading [Vogt, 1971; Jones et al., 2002]. This implies that lithosphere >200 km from the ridge may differ from lithosphere closer to the ridge.

[8] Global tomography models reveal a low-velocity region in the upper mantle beneath Iceland to at least 400 km in depth and along the adjacent MAR for hundreds of kilometers [Bijwaard and Spakman, 1998, 1999; Ritsema et al., 1999; Nataf, 2000; Montelli et al., 2004; Zhao, 2004]. A more detailed regional surface wave study indicates an elongate low-velocity zone extending beneath both Iceland and the MAR [Pilidou et al., 2004] that is confined to the top 200 km of the mantle. Using seismic stations located on Iceland, shear wave splitting measurements yield anisotropy patterns that are interpreted as the result of plume material channeled outward along the ridges [Li and Detrick, 2003; Xue and Allen, 2005]. However, to date no such observations exist along the ridges themselves to verify this interpretation. Seismic anisotropy calculated from Love and Rayleigh waves traveling along the Reykjanes Ridge suggests a vertical alignment of the crystallographic fast axes above 100 km depth, which is interpreted as resulting from buoyant mantle upwelling [Gaherty, 2001].

[9] High levels of primordial volatiles and incompatible elements in Reykjanes Ridge basalts suggest a deeper and more primitive mantle source than for normal MORB. High $^3\text{He}/^4\text{He}$ ratios [Poreda et al., 1986], as compared to normal MORB, are often ascribed to a primitive mantle source, and are present along the Reykjanes Ridge to the Charlie-Gibbs Fracture Zone (a distance of 1700 km from the center of the hot spot). High $^{87}\text{Sr}/^{86}\text{Sr}$ and $^{206}\text{Pb}/^{204}\text{Pb}$, indicators of mantle enrichment, also support hot spot influence to a distance of 1700 km from the center of the hot spot south along the ridge [Taylor et al., 1997]. Major and minor incompatible elements show the greatest enrichment of incompatible elements within ~800 km of the hot spot [Murton et al., 2002], nevertheless Reykjanes Ridge lavas include a contribution of greater than 20% from Icelandic mantle sources at all distances from the plume center [Taylor et al., 1997]. The mechanism of melt transport is not clear from these studies, but it is unlikely that melt is

channeled down the ridge within the crust, because petrologic data show parent melt diversity and a lack of connectivity between crustal magma systems [Murton *et al.*, 2002].

3. Data

[10] The seismic data were recorded on 38 broadband, three-component seismometers deployed as part of the ICEMELT and HOTSPOT experiments, as well as one permanent GSN station (BORG) (Figure 1). The ICEMELT experiment [Bjarnason *et al.*, 1996] consisted of 15 Streck-eisen STS-2 instruments, which were installed across Iceland during 1993–1995 and recorded at a rate of 10 samples per second until the autumn of 1996. The HOTSPOT experiment [Allen *et al.*, 1999] consisted of 30 Guralp CMG3-ESP, 4 Guralp CMG-40T, and 1 Guralp CMG-3T instruments, which were installed during the summer of 1996 and recorded at a rate of 20 samples per second until the summer of 1998. The BORG station contained a Streckeisen STS-2 instrument [Butler *et al.*, 2004; Aster *et al.*, 2005] that recorded at 40 samples per second during the earthquake activity of interest.

[11] Fundamental mode Love (9.5–50 s period) and Rayleigh (14–100 s period) waveforms were collected from 19 earthquakes that occurred south of Iceland with event-station distances ranging from 338 km to 1863 km. After rotation of the horizontal components and correction for instrument responses, the data were narrow band-pass filtered with a Gabor filter [Yomogida and Aki, 1985] to extract discrete fundamental mode wavelets at the center frequency of the filter. The center frequencies used for Rayleigh waves were: 0.01, 0.0128, 0.02, 0.03, 0.04, 0.05, 0.053, 0.055, 0.057, 0.060, 0.065, and 0.070 Hz; for Love waves they were: 0.02, 0.03, 0.04, 0.045, 0.050, 0.055, 0.060, 0.065, 0.070, 0.075, 0.080, 0.085, 0.090, 0.100, and 0.105 Hz. The center frequencies were more closely spaced in regions of the seismic spectrum where phase velocities changed more rapidly. The data were manually reviewed and traces with poor signal-to-noise ratios were discarded. Although the data provide excellent sampling of the mantle beneath the ridge axis and outward to 350 km east of the ridge, there is less coverage >250 km west of the ridge since few large earthquakes occurred to the west during the recording period.

[12] Initial examination of the data indicates lower velocities below the ridge than beneath older lithosphere. Apparent group velocities for Love and Rayleigh waves show an ~8% reduction for paths along the ridge versus paths away from the ridge (Figure 2). Amplitudes of the waveforms exhibit focusing effects, further indication of a subridge low-velocity zone. For events located on the ridge, plots of traces organized in geographic order (west to east) reveal significantly higher amplitudes for stations located near the ridge (Figure 3). This focusing effect could result from lateral refraction of surface wave energy into a low-velocity zone beneath the ridge axis, which acts as a waveguide that traps the surface wave energy [Dunn and Forsyth, 2003]. The amplitude focusing cannot be explained by the radia-

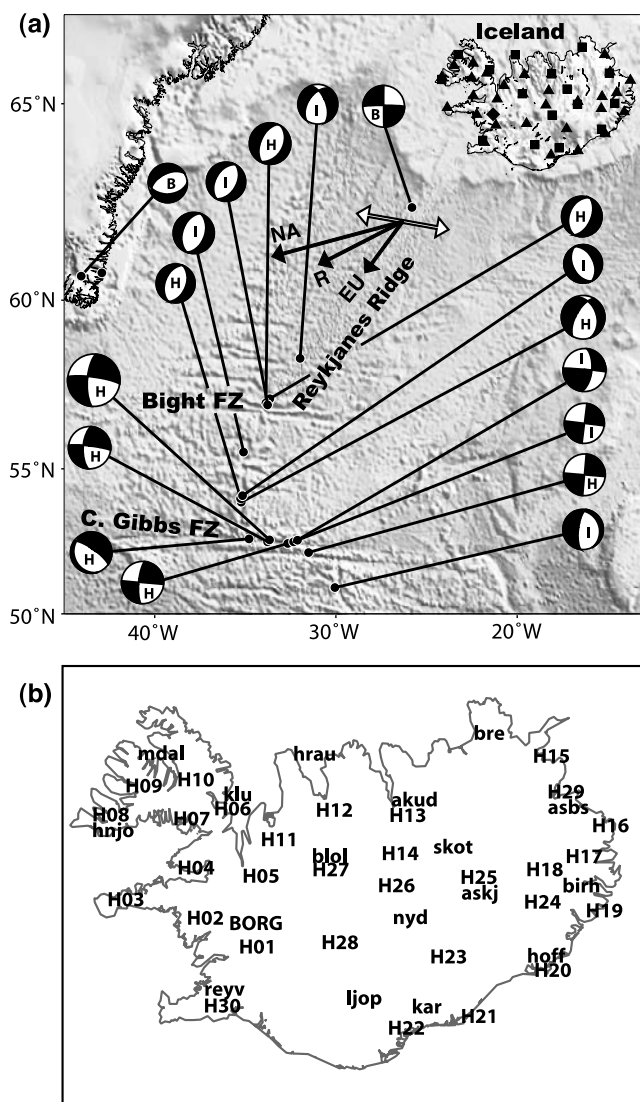


Figure 1. (a) Predicted bathymetry map [National Geophysical Data Center, 1993] of the Reykjanes Ridge showing the location of the ICEMELT array (squares), the HOTSPOT array (triangles), and the BORG station of the Global Seismograph Network (diamond). Also shown are the locations and focal mechanisms of earthquakes used in this study. The focal mechanisms are labeled with “H,” “I,” and “B” for earthquakes recorded by the HOTSPOT and ICEMELT arrays and the station BORG, respectively. The two white vectors with black outlines indicate the relative spreading of the North American and Eurasian plates (~1.9 cm/yr). The vector labeled “NA” indicates the absolute motion of the North American (~2.8 cm/yr) plate, and the vector labeled “EU” indicates the absolute motion of the Eurasian plate (~1.3 cm/yr), both in a hot spot reference frame [Gripp and Gordon, 2002]. The vector labeled “R” indicates the absolute motion of the plate boundary (~1.9 cm/yr) in a hot spot reference frame. (b) Map of Iceland with station names and locations. Stations labeled with an “H” followed by a number are HOTSPOT stations. All other stations, with the exception of BORG, are from the ICEMELT array.

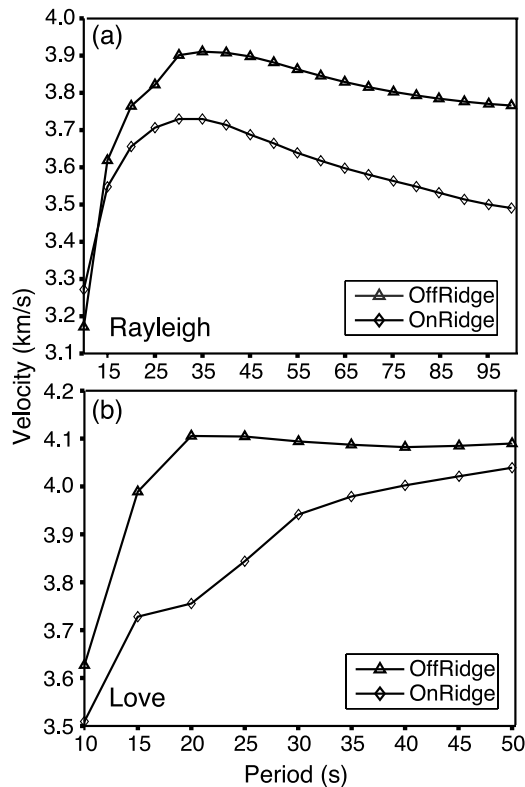


Figure 2. Apparent (a) Rayleigh and (b) Love wave group velocities for raypaths that traveled both near and far from the ridge axis reveal low velocities beneath the ridge. For Rayleigh waves, on-ridge paths are $\sim 3\%$ slower than off-ridge paths at a period of 15 s, increasing with period to $\sim 7.5\%$ slower at a period of 100 s. For Love waves, on-ridge paths are $\sim 3\%$ slower than off-ridge paths at a period of 10 s, $\sim 8.5\%$ slower at 20 s, and only $\sim 1\%$ slower at 50 s. Apparent group velocity is calculated by dividing the event-station distance by the arrival time of the peak of the Love or Rayleigh narrowband wavelet. For on-axis raypaths, events located on the Reykjanes Ridge are paired with stations located near the ridge axis. For off-axis raypaths, events far from the Reykjanes Ridge along the Charlie-Gibbs Fracture Zone are paired with stations located in the far eastern part of Iceland. Data for rays that sample both on and off-axis regions are not included in Figure 2.

tion pattern of the source, which in many cases predicts the opposite effect.

4. Methods

[13] We use the waveform modeling method of *Dunn and Forsyth* [2003], which solves for tomographic images of the anisotropic shear wave velocity structure. This is a two-step method that first uses the phase, group arrival time, and amplitude information of the wavelets to solve for Love and Rayleigh wave phase velocity structure, and then uses the phase velocities to solve for anisotropic shear wave velocity structure. Both steps consist of forward calculations of synthetics and inverse calculations for the solution. Because most of the surface waves traveled roughly parallel to the ridge axis, they provide little sensitivity to along-axis

variations in velocity structure. Therefore, except where otherwise noted, the solution represents an along-axis average of the ridge velocity structure; the tomographic images are therefore constructed in a vertical plane oriented normal to the ridge.

[14] In the first step, the forward problem consists of computing synthetic wavelets at the stations for a given phase velocity structure that is defined on a grid extending 1452 km across the ridge (x axis) and 2200 km along the ridge (y axis). Although modeled phase velocities vary in both x and y, the y axis variation is due simply to the bending of the ridge. North of the Bight Fracture Zone, the ridge is located at $y = 0$. South of the Bight Fracture Zone, the ridge has a slight bend such that the ridge is located at $y > 0$. In this region, distance from the ridge is measured from the actual location of the ridge, not $y = 0$. At any point along the ridge, the phase velocity structure as a function of distance from the ridge is the same. The starting phase-velocity model was derived from phase velocity values of the Pacific upper mantle [*Nishimura and Forsyth*, 1988] using lithospheric ages appropriate for the Reykjanes Ridge. The initial phase and radiation pattern for each event were computed from the double couple solution of the earthquake [see of *Aki and Richards*, 2002, section 7.5].

[15] For the inverse problem, to reduce the number of parameters, the phase velocities at each period were fit to a cubic spline under tension with 15 control nodes defined at distances of 0, ± 50 , ± 100 , ± 175 , ± 250 , ± 350 , ± 500 , and ± 726 km from the ridge axis. At each of these nodes, a dispersion curve was defined as a third-order (for Love waves) or fourth-order (for Rayleigh waves) polynomial. Therefore there were 60 (Love) and 75 (Rayleigh) parameters for phase velocity. The objective of the inverse problem is to solve for the polynomial coefficients at each control node and determine the phase velocity as a function of frequency and distance from the ridge. The data for all frequencies are modeled together in a joint inversion.

[16] For each event, the best available source parameters were extracted from the ISC online bulletin (available at <http://www.isc.ac.uk>), the Global CMT Project (available at <http://www.globalcmt.org>) [e.g., *Ekström et al.*, 2005], and *Engdahl et al.*, [1998] catalogs. Uncertainties in the focal mechanisms, locations, and depths of the events were accounted for in the phase, group, and amplitude uncertainties, which were estimated in a manner similar to that of *Dunn and Forsyth* [2003]. The initial phases for Rayleigh waves had negligible sensitivity to the uncertainties in event depth, but for some Love wave sources a depth difference of 5 km could shift the phase by $\pi/9$ or more. However, in most cases the uncertainty was less than $\pi/30$, which corresponds to <0.01 km/s error in phase velocity for a single 25 s wave recorded on Iceland. The combined uncertainty in the phase velocity structure due to uncertainties in the event locations (<10 km) is <0.01 km/s. Although event depth affects the absolute amplitude of Love waves, this method only models relative amplitudes across the array at each center frequency. For Rayleigh waves, the depth sensitivity was only important when the event was shallow (<8 km). While uncertainties in the focal mechanism could affect the relative amplitudes across the arrays, the source radiation patterns for all but the longest periods is a secondary signal to the focusing and defocusing of energy

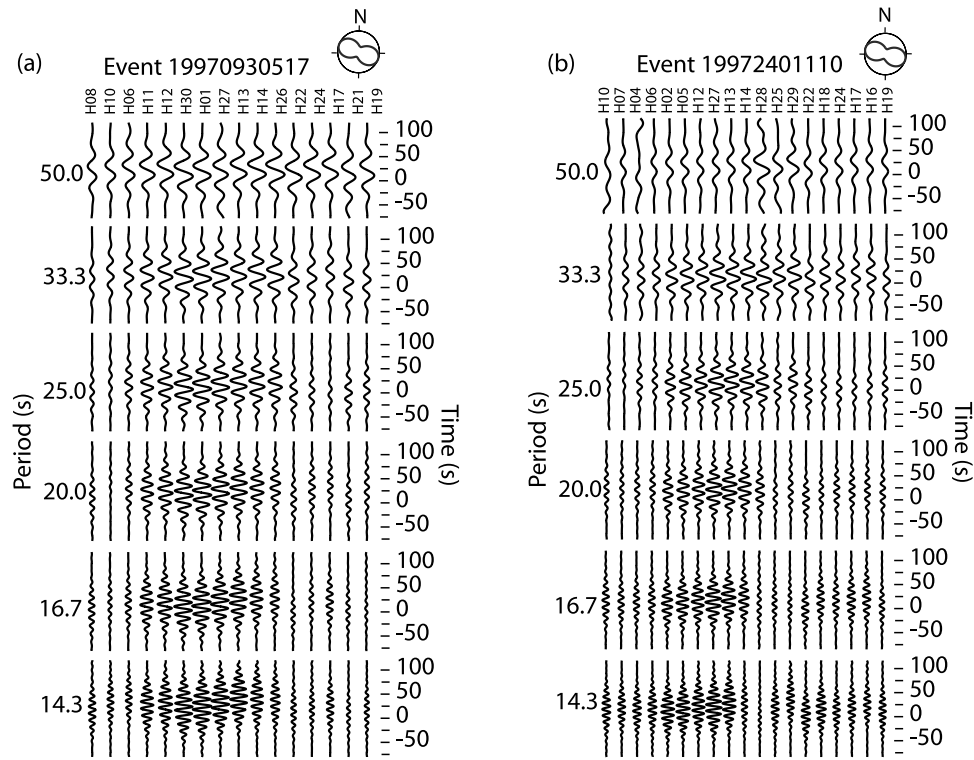


Figure 3. Rayleigh wave traces (period of waves indicated on plots) for two representative on-axis earthquakes showing amplitude focusing for energy traveling along the Reykjanes Ridge. The event-station distance is (a) ~ 1000 km for event 19970930517 and (b) ~ 1400 km for event 19972401110. The timing of the traces is corrected for distance and shown in geographic order from west to east. A low-velocity region beneath the ridge acts as a waveguide that traps the energy of the Rayleigh waves. Wave focusing increases with decreasing period, indicating that waves at lower periods are sensing greater lateral variations in phase velocity; at the lowest periods the amplitude pattern becomes more chaotic because of increased scattering, especially for the more distant event. This wave focusing cannot be accounted for by the radiation pattern of the source mechanisms (shown at the top right of each plot).

due to the subridge waveguide (at long periods the focusing effect is small). Amplitude uncertainties due to focal mechanism uncertainties are azimuthally dependent, but trends in the amplitudes across the seismic array are only marginally affected by this uncertainty. We do not solve for attenuation structure and lateral variations in attenuation could affect amplitudes and hence our result. This is largely offset by the fact that we model relative amplitude variations across the array for individual events, which have similar paths, and we do not model relative differences between events [see *Dunn and Forsyth, 2003*]. We can estimate a maximum effect using a single event located at 1200 km from the array on the ridge. For event-to-station paths in this study, a reasonable guess as to the maximum variation in Q is 100 versus 250 in the upper 50 km of the mantle. For a 25 s period wave, the amplitude difference is 23%, which is approximately the minimum assigned uncertainty to the measured amplitude values. This difference decreases significantly with increasing period. At periods most sensitive to the sublithospheric region (60–70 s), a large Q variation from 80 to 150 produces a small 10% amplitude difference. In general, the tendency will be to underestimate the degree of energy focusing. Also, given the relatively larger uncertainties for the amplitude and group information, the phase information is the strongest constraint on the solutions.

[17] It was necessary to forward model the data first, starting with the longest period waves, to avoid a 2π phase ambiguity. Then, a joint solution for all periods and for all of the Love or Rayleigh data was accomplished via several iterations of the forward and inverse problems. The chi-squared misfit of a solution was determined from differences between the phase, amplitude, and group arrival time of the observed and calculated waveforms. Uncertainties in the phase velocity solution were estimated from a linearized error propagation approach and additional sensitivity tests, as discussed below.

[18] In the second step, the anisotropic shear wave velocity, as a function of depth and distance from the ridge, was calculated via a joint inversion of the Love and Rayleigh wave phase velocities. The solution was calculated in a vertical plane extending 1200 km across the ridge and 600 km in depth (although our maximum depth of resolution is ~ 200 –250 km). After *Takeuchi and Saito [1972]*, we solve for V_{SV} (the velocity of a vertically polarized shear wave) and ξ (where $\xi = (V_{SH}/V_{SV})^2$ and V_{SH} is the velocity of a horizontally propagating, horizontally polarized shear wave). Compressional wave velocity and density are also calculated as part of the inversion. However surface waves in the period range used here are insensitive to these parameters [*Nishimura and Forsyth, 1988*] and their solu-

Table 1. Starting Model

Layer Thickness, km	V_P , km/s	V_{SV} , km/s	Density, kg/m ³
Water ^a	1.5008	0	1.04
Sediment ^a	2.0	1.5	1.5
2	5.6	3.1	2.6
3	6.4	3.4	2.8
5	7.2	3.7	3.0
5	8.4	4.54	3.330
5	8.4	4.48	3.330
6	8.3	4.42	3.330
7	8.2	4.37	3.340
8	8.1	4.31	3.350
9	8.0	4.26	3.360
10	7.8	4.20	3.370
10	7.8	4.16	3.370
10	7.8	4.12	3.370
10	7.8	4.11	3.370
10	7.9	4.10	3.373
15	7.9	4.11	3.376
15	8.0	4.13	3.400
15	8.1	4.18	3.440
20	8.1	4.25	3.440
30	8.1	4.30	3.440
40	8.2	4.35	3.475
50	8.4	4.40	3.501
60	8.6	4.50	3.515
65	8.6	4.60	3.515
80	9.2	5.00	3.680
100	9.6	5.25	3.820

^aSediment and water layer thicknesses vary.

tions deviated little with respect to the starting model. For the results presented below, the percent anisotropy is defined as $100 \cdot (V_{SH} - V_{SV}) / V_{average}$. This type of anisotropy is often referred to as “transverse isotropy” (hexagonal symmetry with a vertical symmetry axis) [Babuska and Cara, 1991].

[19] The forward problem consists of computing synthetic dispersion curves and partial derivatives relating changes in the dispersion curves to changes in the velocity structure and anisotropy for each column of the 2-D model and then comparing synthetic dispersion curves to the dispersion curves determined in step one. The isotropic 1-D, depth-varying, starting model used for the 2-D solution (Table 1) was determined by solving for the best 1-D model that satisfied all of our data; while the starting model for this 1-D solution was a 1-D model determined from the results of Gaherty [2001]. We did not use the Gaherty [2001] solution as our starting model, since we include shorter-period data that require, on average, higher velocities at the top of the mantle than are present in the Gaherty model. If we use the Gaherty model as a starting model, it yields a higher initial data misfit and produces similar, but spatially rougher, solutions. Crustal thickness is not well known, so a range of reasonable values was tried by altering the thickness of the deepest crustal layer. A value of 10 km total thickness resulted in the best overall fit to the data. Layer thickness is uniform across the model, except for the water depth and sediment layer, whose thicknesses were determined by averaging known values along the ridge [National Geophysical Data Center, 1993, 2005].

[20] The inverse problem consists of solving for the model parameters subject to penalty constraints on their magnitude and spatial roughness. The penalty constraints

are applied as additional rows to the matrix of partial derivatives that relate phase velocities to the model parameters [e.g., Nolet, 1987]. The 2-D solution at each iteration of the problem is computed via the LSQR method [Paige and Saunders, 1982]. We apply equal “roughness” to the different model parameters, such that we calculate the smoothest models that fit the data. Of importance to the resolution of the images is any trade-off between isotropic shear wave velocity and anisotropy. This trade-off is controlled by the parameter, η , a ratio of the penalty constraints on V_{SV} versus ξ , as discussed below.

5. Results

5.1. Rayleigh Wave Phase Velocity

[21] Rayleigh wave phase velocities (Figure 4a), are $\sim 4\text{--}6\%$ slower beneath the ridge than away from the ridge. The low phase velocity zone is 250 km wide at short periods ($< \sim 25$ s) and much broader at longer periods. Phase velocities are asymmetric about the ridge, with higher velocities to the east at shorter periods and higher velocities to the west at longer periods. We tested the significance of the asymmetry by comparing this solution to one that was generated with a symmetry requirement, an f test indicates that at the 99% level of confidence the velocity structure is not symmetric.

[22] Phase velocity variations along the ridge are small compared to the uncertainties of the data and solution. Solutions that allow a linear gradient in phase velocities along the ridge did not result in lower misfits. Figure 5 contains traces from four earthquakes with event station distances of $\sim 838\text{--}1850$ km; the traces show no significant difference in fit with the synthetics. On the other hand, on Iceland the region around the center of the hot spot has a significant effect on seismic energy that crosses it (Figure 6). After first correcting for the along-axis average phase velocity model shown in Figure 4a, short-period energy crossing this region has measurable phase delays as compared to energy recorded on the nearside of the region. On the other hand, stations located on the far side of Iceland that do not have event-station paths that cross the center of the hot spot record negligible delays. To remove this local effect, data for waves that cross the region near the hot spot center were removed from our final results.

[23] A common method for computing solution variance for linearized problems is described by $C'_m = C_m - C_m G_\infty^t (G_\infty C_m G_\infty^t + C_d)^{-1} G_\infty C_m$, where C'_m is the solution covariance matrix, C_m is the initial model covariance, C_d is the data covariance, and G_∞ is the final partial derivative matrix [Tarantola, 1987]. However, this method may underestimate the actual solution variance for our nonlinear problem, even though the character of the distribution of the resulting values appears correct (i.e., large uncertainties far from the ridge and relatively larger values to the west than the east). Uncertainties calculated via this linearized method were thus scaled based on additional sensitivity tests. Randomly perturbing the final solution and recalculating the solution misfit indicates that multiplying the uncertainties from the above method by a factor of five gives a better approximation to actual uncertainties. The standard deviation for Rayleigh wave phase velocity (Figure 4a) is < 0.05 km/s for all periods at distances

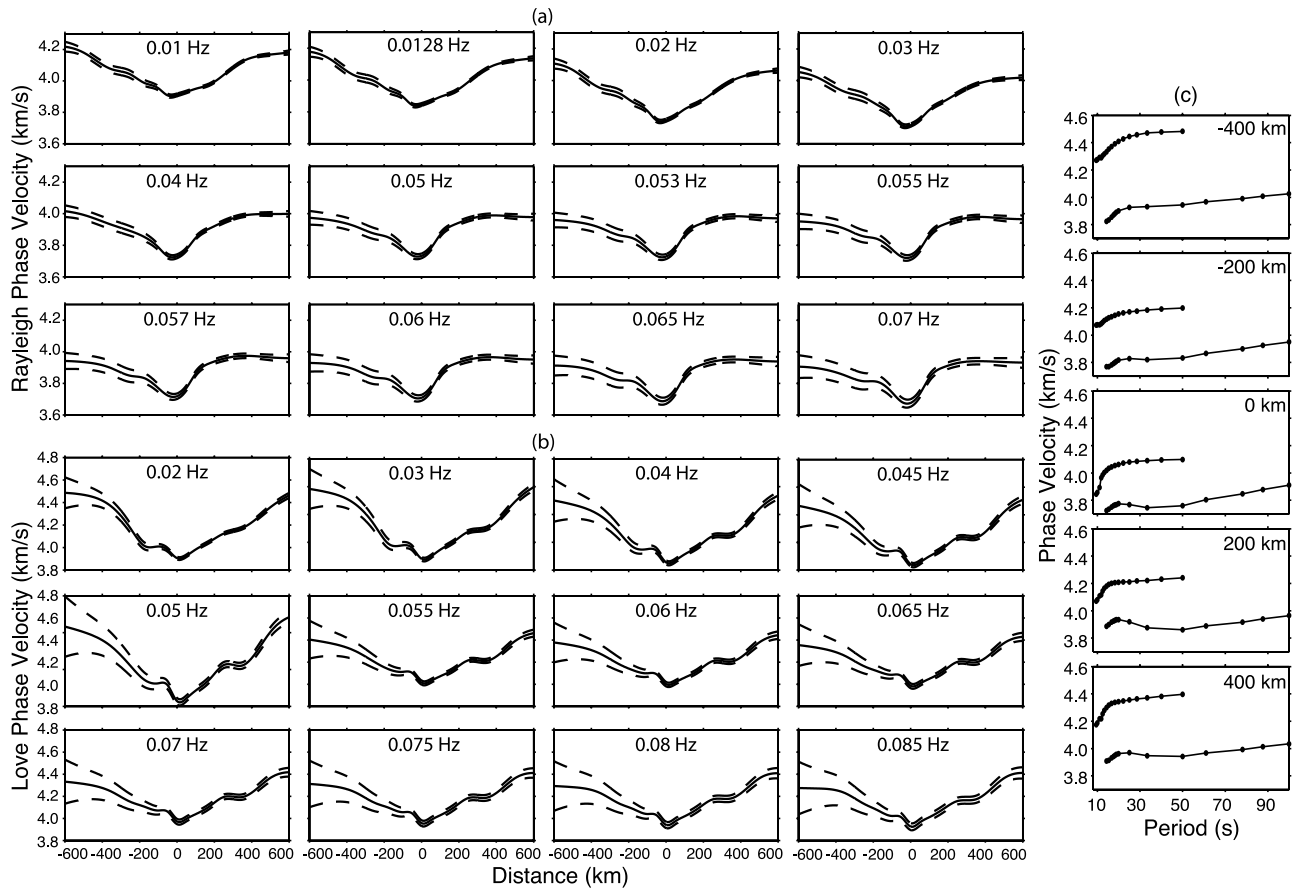


Figure 4. Plots of the (a) Rayleigh and (b) Love phase velocity solutions (solid curves), along with their corresponding standard deviations (dashed curves). The horizontal axis represents distance from the ridge axis. Each phase velocity curve is computed for the center frequency of the wavelets (indicated on each plot). Phase velocities are computed using the phase, amplitude, and group velocity of the wavelets (amplitude is sensitive to the spatial curvature of the phase velocities, and group velocity is sensitive to the variation in phase with frequency). (c) Phase velocity dispersion curves at select distances across the ridge (positions noted on plots). In each case the top curve is for Love waves, and the bottom curve is for Rayleigh waves.

between -100 to 500 km and east of -500 km for periods of 25 s and higher. To the west of -100 km at periods of less than 25 s the standard deviation is between 0.05 and 0.10 km/s except >250 km west of the ridge, where it is >0.1 km/s for all periods.

5.2. Love Wave Phase Velocity

[24] Love wave phase velocities show similar features to their Rayleigh counterparts. However, there is no reason to expect closely similar patterns since the two wave types have different depth sensitivity and response to anisotropy. Love wave phase velocities (Figure 4b) also decrease toward the ridge axis and are $\sim 9\%$ slower at the ridge than farther away, depending on period. Superimposed on the general trend is a narrower low-velocity zone centered approximately beneath the ridge. There is no detectable ridge-parallel variation. Phase velocities are asymmetric: at distances <100 km from the ridge the velocities are greater on the western side, at greater distances the velocities are greater on the eastern side. An f test comparing symmetric and asymmetric models indicates that the phase velocities are asymmetric at the 99% level of confidence. Using the

same method as for the Rayleigh case, the standard deviation for Love phase velocities is <0.06 km/s for all periods at distances between -100 to 450 km, for all periods 14.28 s and above at all distances farther east than 450 km, and for periods 20 s and above for all distances east of -400 km (Figure 4b). To the west of -400 km, the standard deviation exceeds 0.06 km/s for all periods.

5.3. Shear Wave Velocity and Anisotropy

[25] We present a set of solutions in Figures 7a–7c that differ by the ratio η , which controls the importance of fitting the data with shear wave perturbations versus anisotropy. The value of η is equal to 1, $1/2$ (anisotropy more important), and 2 (V_{SV} more important), for Figures 7a, 7b, and 7c, respectively. Values of η larger than 2, or smaller than $1/2$, do not result in models that fit the data. Each of the shear wave solutions (left panels) exhibits a high-velocity lithospheric lid at the top of the mantle that thickens with lithospheric age and a wide and deep low-velocity zone in the upper mantle approximately centered beneath the Reykjanes Ridge. The corresponding anisotropy solutions (right panels) contains a variable pattern with $V_{SH} > V_{SV}$ at

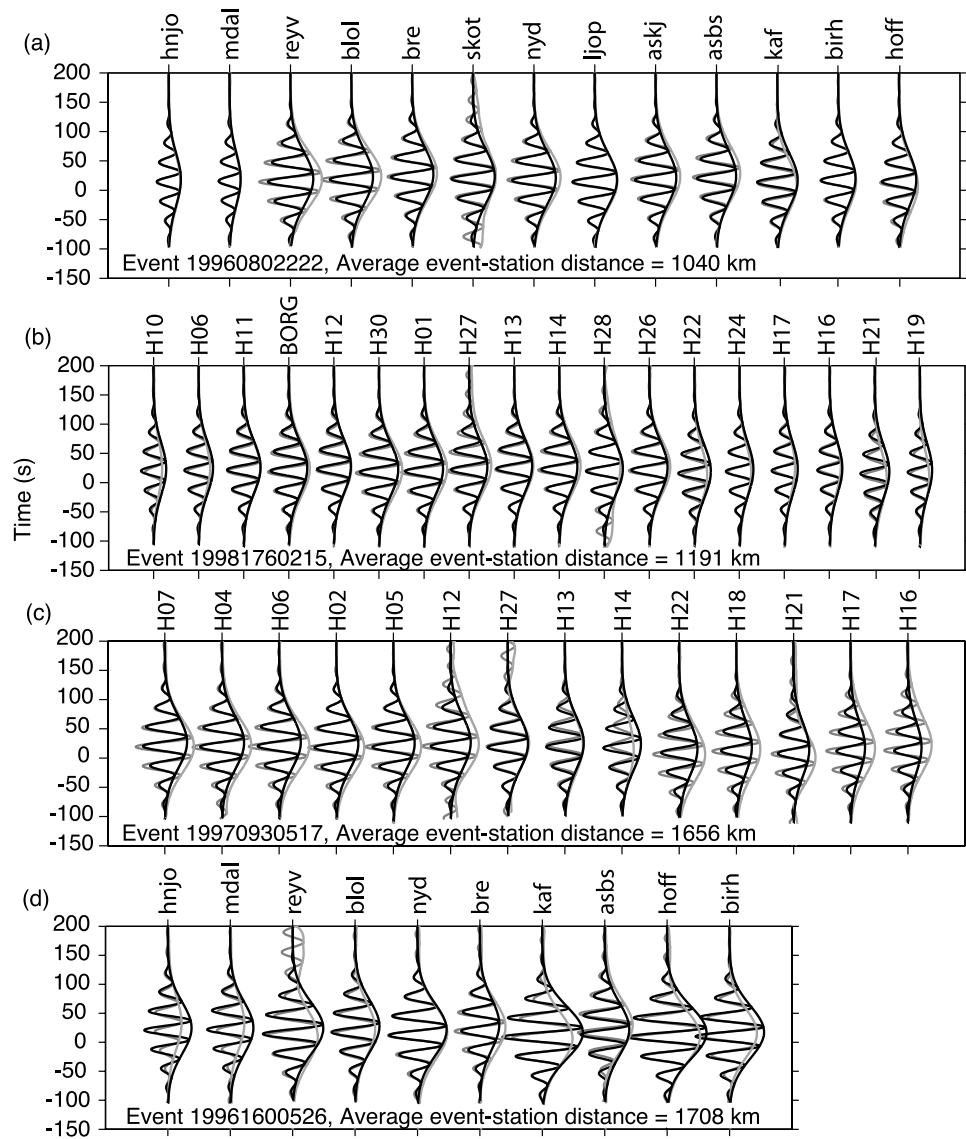


Figure 5. Rayleigh waveforms (33 s period) for four events that occurred along the Reykjanes Ridge but at different distances from Iceland. The average event-to-station distances are (a) 1040, (b) 1191, (c) 1656, and (d) 1708 km. The synthetic data for our phase velocity solution (solid curves) have the same statistical fit for each of these events (shaded curves). Thus any along-axis variation in phase velocity is too small to be detected by this study.

distances >200 km from the ridge, and $V_{SV} > V_{SH}$ in a broad asymmetric region within ± 200 km of the ridge. While the three solutions have similar features, the features do vary in magnitude (e.g., a solution calculated with a weaker constraint on anisotropy has larger anisotropy magnitudes). Overall, the images are similar enough that the subsequent interpretation of the images (below) is unaffected.

[26] Most of the variation observed in the phase velocities translates into lateral variations of the shear wave solution at depths <75 km and corresponds with the high-velocity lithospheric lid, at the top of the mantle, which thickens asymmetrically with age such that a thinner lid with lower velocities is observed on the western side. Beneath the lithospheric lid, the low-velocity anomaly extends to at least 250–300 km from the ridge (lithospheric ages of 30+ Ma). In terms of lithospheric age the anomaly is

>10 times wider than that beneath the fast spreading southern East Pacific Rise (EPR), which extends out to lithospheric ages of only 1.5–3 Ma [Toomey *et al.*, 1998; Hammond and Toomey, 2003]. Sensitivities of the surface waves to the velocity structure have long downward tails (Figure 8). The long decay in sensitivity with depth makes it difficult to determine the depth extent of the anomalous sublithospheric velocity structure. We examined the depth extent of the low-velocity anomaly and anisotropy by decreasing the allowed horizontal roughness at the bottom of the model in order to force any lateral variations to shallower depths. By examining the misfit of the data for these squeezed models, this test determined the depth constraints that the data can place on the structure. A squeezing boundary at 135 km depth results in V_{SV} (Figure 7d left) and anisotropy solutions (Figure 7d right) with data misfits on par with that of

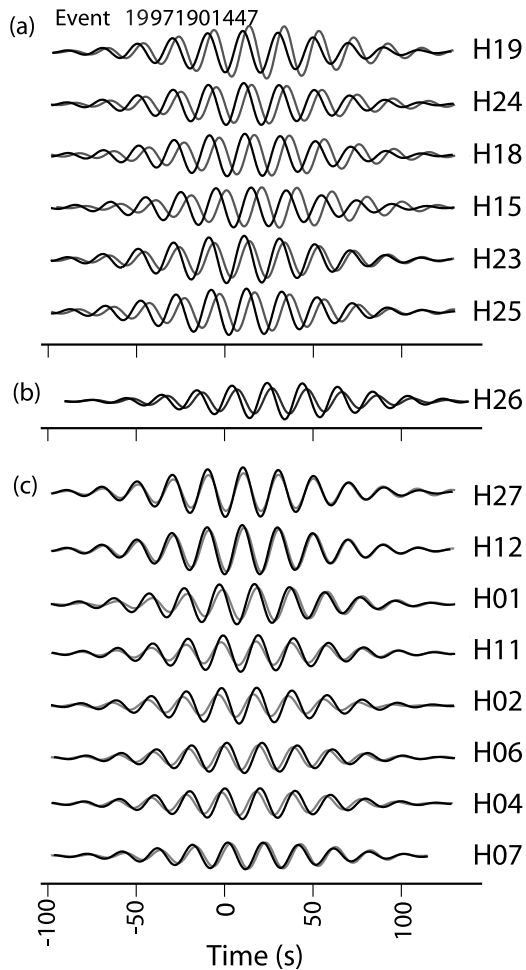


Figure 6. An examination of data and synthetics for waves recorded on stations across Iceland revealing the effects of unmodeled structure around each station. Here we show data (shaded curves) and synthetics (solid curves) for 20 s Rayleigh wavelets; the synthetics are calculated for our axially invariant phase velocity solution. (a) Traces from stations that are behind the center of the hot spot, thought to be near Griacutemsvötn Volcano [Einarsson *et al.*, 1997], delayed compared to synthetic traces generated from our axially invariant velocity model. (b) A trace recorded near the north of Iceland, but not behind the center of the hot spot, showing only a slight delay. (c) Traces for stations located on the nearside of Iceland (southern and western side) showing no delay. On the basis of these observations we did not include data such as that shown in Figure 6a to compute our final solutions.

Figures 7a–7c ($\chi^2 < 1$). As the squeezing boundary is moved upward, the misfit increases; a depth of 100 km (Figure 7e) is approximately the shallowest depth for which the solution still reasonably fits the data.

[27] Measurable anisotropy is limited to the upper ~150 km of the mantle. Our results generally agree with the earlier work by Gaherty [2001], except that these higher-resolution results reveal greater detail. At distances >200 km from the ridge and shallow lithospheric depths (<50 km), V_{SH} is much greater than V_{SV} with a magnitude <5%. At distances >300 km from the ridge, this form of

anisotropy is found to 100–150 km depth. The magnitude is probably less well constrained than Figures 7a–7d indicate, because of the depth averaging of the surface waves. The large increase in magnitude at distances greater than 350 km from the ridge should be viewed with suspicion because of a drop in data coverage and model resolution. In the broad region beneath the ridge where $V_{SV} > V_{SH}$, the anisotropy pattern is strongly asymmetric, with a magnitude of up to 4.5% between 0 and 200 km east of the ridge and up to 1.5% between 100 and 200 km west of the ridge. The region of strongest anisotropy (most negative in Figure 7) is significantly shallower than the region of slowest velocities; it is within the lithospheric lid, significantly east of the ridge axis. Our result does not contain $V_{SV} < V_{SH}$ below 100 km in depth near the ridge as suggested by Gaherty [2001]. The reason for this may be that we were unable to use the longest-period Love wave data used by Gaherty [2001] (>50 s) because of insufficient coverage of these data across our experimental region.

6. Physical Interpretation of the Seismic Structure

[28] From our velocity structure, we calculated a thermal model (Figure 9a) using a self-consistent method for temperature, shear modulus, and density [Faul and Jackson, 2005]. We performed a grid search to find the temperature values that give density and shear modulus values that are consistent with our seismic structure. For this modeling we used a temperature- and pressure-dependent coefficient of thermal expansion [Schmelling *et al.*, 2003] and the physical constants given by Faul and Jackson, including a grain size of 1 mm and a potential temperature of 1400. Since the Faul and Jackson calculations are frequency-dependent, we used the depth sensitivities of the surface waves to weight the importance of different frequencies with depth. Grain size and potential temperature affect the temperature values calculated, but have only a modest effect on the lateral temperature contrasts at each depth. The Faul and Jackson calculations, in which velocity is controlled solely by the elastic and anelastic effects of temperature changes, predict much lower Q values than measured near ridges [e.g., Yang *et al.*, 2007]. In other words, in order to fit the velocity data without the additional effects of melt or water these calculations require very low Q and high temperatures. This discrepancy indicates that a small amount of melt/water is broadly distributed everywhere beneath lithospheric lid, which partly gives rise the asthenospheric low velocities. Thus the average sublithospheric temperatures need not be as high shown in Figure 9a. On the other hand, lateral temperature variations may still be reasonably estimated via this technique.

[29] At the top of the mantle (<30 km below the crust), we find lateral temperature variations up to 1100°C. Such large variations are reasonable considering that they reflect the cooling of the lithosphere with age. While there is no obvious way to compute the effective lithospheric thickness from a seismic velocity profile, if we define the base of the lithosphere as the depth of maximum negative gradient of $V_{average}$ [e.g., van der Lee, 2002; Gu *et al.*, 2005], then 10 Ma lithosphere is 26 km and 40 km thick to the west and east of the ridge, respectively. In comparison, a half-space

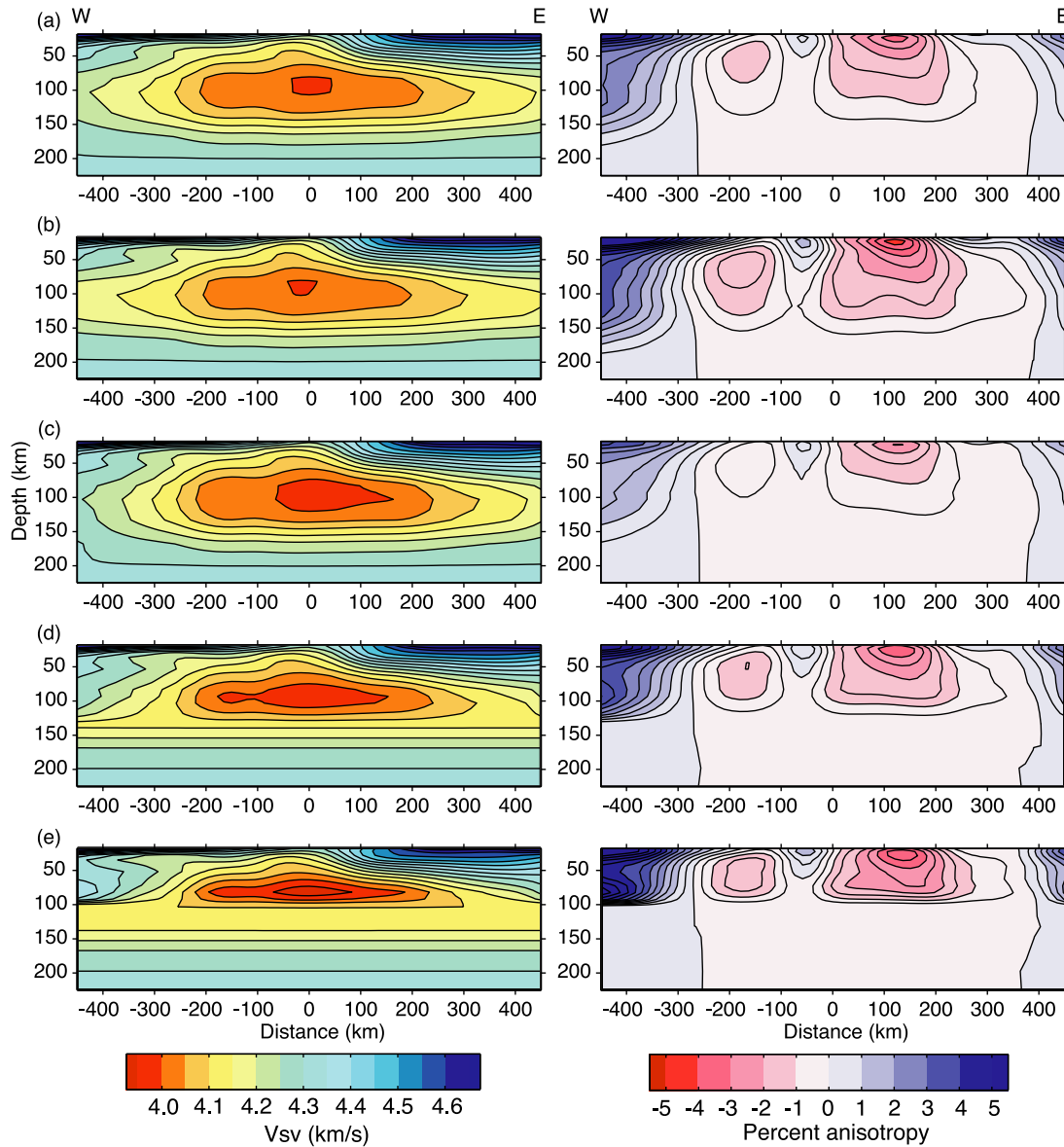


Figure 7. Tomographic images of (left) shear wave velocity, V_{SV} , and (right) percent anisotropy. Shear wave velocity and anisotropy are calculated together in a joint inversion of the Love and Rayleigh wave phase velocities (shown in Figure 4). The images are oriented in a vertical plane, normal to the ridge axis; the horizontal axis indicates the distance from the ridge axis; the vertical axis indicates depth below the seafloor. The magnitude of anisotropy is defined as $100(V_{SH} - V_{SV})/V_{average}$, where V_{SH} is the shear wave velocity of a horizontally polarized shear wave, V_{SV} is for a vertically polarized shear wave, and $V_{average}$ is the average of the two. Ratio, η , of the penalty constraints on V_{SV} versus ξ (the anisotropy parameter): (a) 1, (b) 1/2, and (c) 2. A smoothness constraint added below (d) 135 and (e) 100 km that squeezes lateral variations in velocity or anisotropy structure to shallower depths ($\eta = 1$ used in both cases). See text for discussion.

cooling model [Turcotte and Schubert, 2002] (calculated using a thermal diffusivity of 10^{-6} W/m² and an adiabat calculated with variable compressibility [Schmelling et al., 2003]) predicts a lithospheric thickness of 41 km at 10 Ma. Thus the North American plate is much thinner than expected.

[30] Beneath the lithosphere, we predict a $\sim 75^\circ\text{C}$ thermal anomaly over a broad region centered beneath the ridge. This value is similar to estimates of anomalous mantle

temperatures based on a geochemical study of rare earth elements in Reykjanes Ridge basaltic rocks ($<100^\circ\text{C}$ [White et al., 1995]). Note that the temperature anomaly in Figure 9a exhibits a thermal inversion in the mantle, where higher temperatures overlie slightly cooler temperatures. On the other hand, the low-velocity region could instead be caused by lateral variations in melt fraction. Assuming relaxed moduli and that melt is organized in tubules at fractions less than 1% and in films and tubules above 1% [Hammond

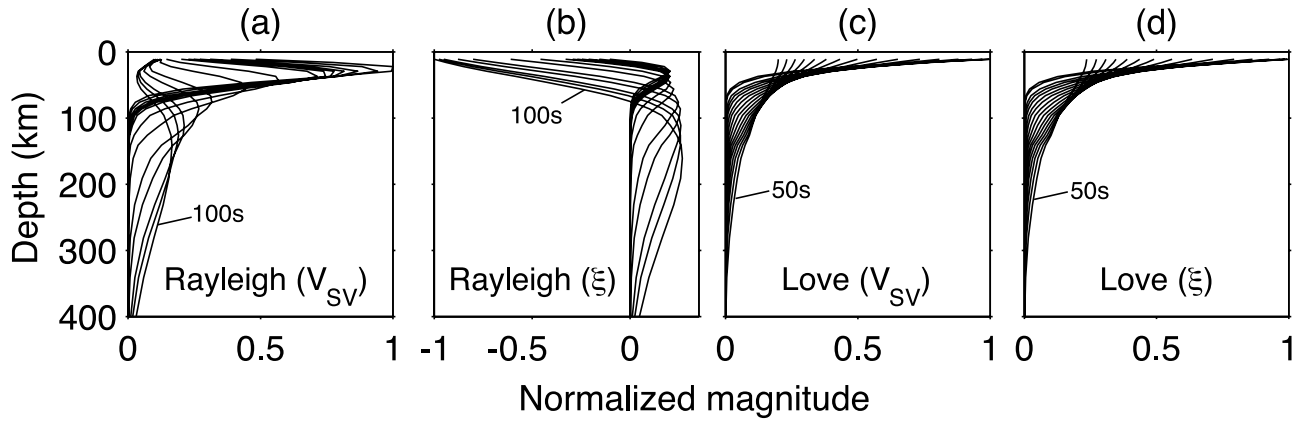


Figure 8. Normalized V_{SV} and $\xi (=V_{SH}^2/V_{SV}^2)$ sensitivities to (a and b) Rayleigh and (c and d) Love phase velocities as a function of depth. Values plotted are spatial averages across the entire region of study. Each curve represents a single period (varying uniformly from 9.5 to 50 s for Love and 14 to 100 s for Rayleigh waves) and shows how phase velocity information is mapped into V_{SV} and ξ structure. Since Love waves have horizontal displacements, the sensitivity to V_{SH} combines that of V_{SV} and ξ .

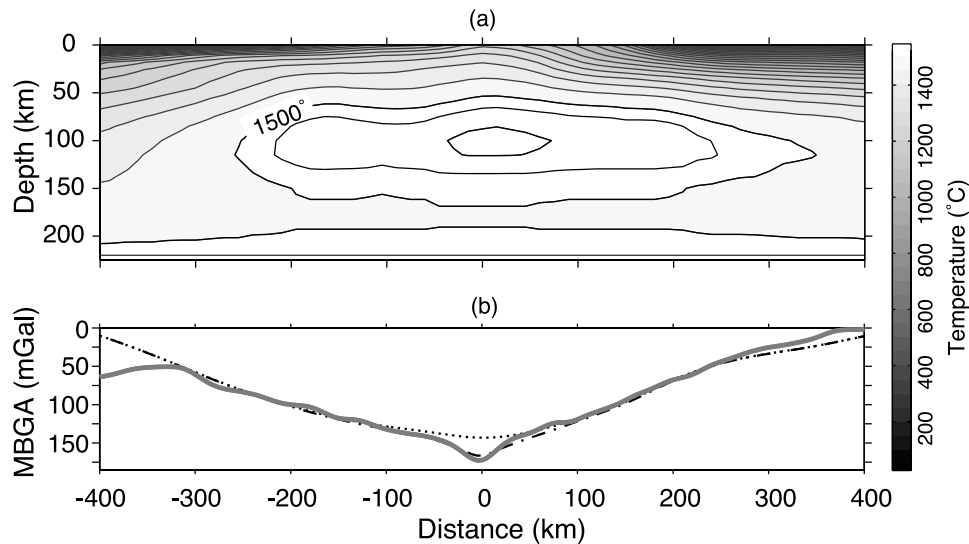


Figure 9. (a) Temperature distribution predicted if the shear wave velocity structure (from Figure 7a) is assumed to be due entirely to variations in temperature. To more clearly show the sublithospheric temperature anomaly, temperatures greater than 1500°C are contoured at 25° intervals, while below 1500° they are contoured at 50° intervals. Note the relatively high temperatures at the top of the mantle just beneath the ridge axis ($x = 0$ km) and the deepening of the isotherms away from the ridge at lithospheric depths. Our results are consistent with a very broad and deep high-temperature region ($\sim 75^{\circ}$ anomaly) beneath the lithosphere, as might occur for broad southward plume flow away from Iceland. For clarity, the water and crust are not shown, and there is a small vertical exaggeration. The temperature modeling suggests a thermal inversion in the mantle, with temperatures at 100 km depth being $\sim 50^{\circ}$ – 75°C hotter than at 175 km depth. (b) Mantle Bouguer gravity anomaly shown by the solid line (data from Dater *et al.* [1999], anomaly calculated with a variable thickness sediment layer [National Geophysical Data Center, 2005] and a three-layer, 10 km thick crust, see Table 1). The anomaly has been averaged along the ridge to produce a single profile; the 95% confidence interval of the mean is less than ± 1 mGal everywhere across the profile. Synthetic mantle Bouguer gravity anomaly calculated from a density structure that is determined by the joint temperature, density, and velocity calculation is shown by the dotted line (see text). Dashed line is the same as for the dotted line, except that a small additional density anomaly was added to the crust and uppermost mantle to fit the extra gravity anomaly at the ridge axis (see text). The thermal structure predicts a gravity signal that closely matches the observed data and indicates that the sublithospheric velocity anomaly is of a thermal origin.

and Humphreys, 2000], the sublithospheric seismic anomaly could be due to an increase in melt fraction beneath the ridge of up to 1%, over whatever the background amount of melt may be in the asthenosphere.

[31] One way to narrow the range of interpretations is to compare gravity data with synthetic values calculated from temperature and melt distribution models that are based on the seismic results. We gathered gravity data [Dater *et al.*, 1999] between the Reykjanes Peninsula and the Bight Fracture Zone and corrected for water depth, sediment thickness (2450 kg/m^3), and a three-layer, uniform thickness crust (see Table 1). By averaging values along the ridge, we constructed a single profile, oriented perpendicular to the ridge, of the mantle Bouguer gravity anomaly (Figure 9b).

[32] Using the mantle density model that was calculated jointly with our thermal model, as outlined above, we then computed synthetic mantle Bouguer gravity values [Talwani *et al.*, 1959]. The results are sensitive to the coefficient of thermal expansion used to calculate the density model, but we found that the values given by the Schmelling *et al.* [2003] method closely predict the observed Mantle Bouguer gravity profile (Figure 9b). Both the asymmetry in the gravity data across the ridge and the amplitude of the signal are well matched, except for a small region just at the ridge axis where there is a 25 mGal, unmodeled, gravity anomaly. Assuming that the sublithospheric temperature anomaly is instead due to melt significantly underpredicts the gravity anomaly, since melt fraction has a large affect on seismic velocities but only a small affect on gravity. In other words, the small amounts of melt predicted by the seismic results give rise to an inconsequential gravity anomaly (to calculate density models for melt fraction models, we simply replaced the appropriate percentage of solid mantle, 3300 kg/m^3 , with melt, 3000 kg/m^3). We rule out compositional effects due to mantle depletion as having any significant bearing on these calculations, since they are expected to be small and while depletion is expected to decrease mantle density [Jordan, 1979], it also weakly increases seismic velocity, and this is inconsistent with our results. The small, 25 mGal, anomaly at the ridge axis possibly arises from the crustal magmatic system and the upper ~ 20 kilometers of the mantle, where our seismic resolution is not sufficient to image small, but perhaps strong, variations in physical properties. The thermal structure and melt content of East Pacific Rise (EPR) crustal magmatic system, as estimated by Dunn *et al.* [2000], can produce a 10 mGal anomaly. Another 15 mGals could be generated by additional cooling of the crust and upper mantle away from the ridge that is not part of the EPR model and by extending the high temperatures and melt fraction at the bottom of the EPR structure several kilometers into the upper mantle. In summary, we find that the combined seismic and gravity data are most consistent with large lithospheric thermal variations and a sublithospheric temperature anomaly of about 75°C . Given that Q values are greatly under predicted, melt (or water) is probably broadly distributed in the asthenosphere here. However, the lateral variation in melt/water content must be small (no more than a couple tenths of a percent) or it would be inconsistent with the combined gravity and seismic analysis.

[33] Anisotropy in the upper mantle is typically attributed to the alignment of olivine crystals due to shear deformation

as a result of mantle flow, such that the crystal a axes align approximately in the shear plane in the direction of mantle flow [Hess, 1964]. The degree of lattice alignment, and thus the bulk magnitude of the anisotropy, increases with strain [e.g., Kaminski and Ribe, 2002]. In our study, the Love-Rayleigh wave anisotropy does not indicate the orientation of the fast axes, nor directly the magnitude of any alignment. Instead, the Love-Rayleigh anisotropy with $V_{SV} > V_{SH}$ has at least two interpretations in terms of mantle fabric: (1) It indicates that faster axes of crystals are predominantly vertically aligned, or (2) it indicates that fast axes are predominantly horizontally aligned in a direction parallel to the ridge axis (rather than the ridge-perpendicular direction typically found in the ocean basins) [Maupin, 1985]. For peridotite elasticity tensors measured from ophiolite rocks and xenoliths [e.g., Kawasaki and Kon'no, 1984; Ben Ismail and Mainprice, 1998], the latter effect is weak, and for this reason Gaherty [2001] interpreted the anisotropy in terms of vertically oriented fabric. The apparent anisotropy would be greater in the second scenario if the ridge-parallel fast axis alignment is accompanied by a predominant alignment of the slow and intermediate axes of olivine, rather than a random distribution about the a axis. Such an alignment, which gives rise to orthorhombic symmetry of the anisotropy pattern, has been detected in experimental studies [Zhang *et al.*, 2000] and natural samples [e.g., Ben Ismail and Mainprice, 1998]. In this case, the intermediate velocity [001] axis aligns within the flow plane, perpendicular to the flow direction, and the slow [010] axis is perpendicular to the shear plane. To enhance the apparent anisotropy, and better explain the data under the second scenario, this mechanism requires along-axis flow with a vertical shear plane.

[34] An alternative interpretation of the observed anisotropy with $V_{SV} > V_{SH}$ is that it arises because of melt distributed in vertically oriented sheets. Deformation experiments of olivine containing small amounts of partial melt indicated that melt may organize into sheets at an oblique angle to the shear direction [Holtzman *et al.*, 2003], separated by relatively melt-free bands containing olivine fabric oriented perpendicular to the shear direction. The heterogeneous melt distribution will produce an apparent anisotropy in waves with different polarizations [Backus, 1965], in addition to the anisotropy due to the olivine fabric. Holtzman *et al.* [2003] suggest that the combination of these effects might be able to explain Gaherty's [2001] Reykjanes data and thus our observations, specifically if channelized flow along the axis occurs with a strong shear plane on a near-vertical "wall" at the edge of the lithosphere. However, the location of the strongest anisotropy within the cooling lithosphere (Figure 7) and the inconsistency of our results with significant amounts of melt suggest that partial melt is not a significant contributor to the anisotropy. The anisotropy may be consistent with fabric formed between segregated melt channels during along-axis flow, and once the melt is removed, the vertical fabric remains.

[35] Our pattern of anisotropy indicates predominantly horizontally aligned fast axes at shallow depths within the high-velocity lithospheric lid at distances of ≥ 200 km away from the ridge. This is typical of oceanic lithosphere in many regions, and can be explained by ridge-perpendicular alignment of the fast axes in the horizontal plane due to

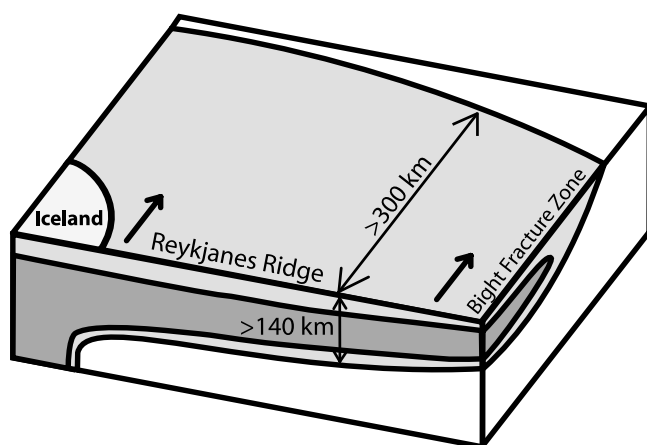


Figure 10. A simple cartoon interpretation of our seismic results. Our results indicate that a thermal anomaly fills the upper mantle over a broad region beneath the North Atlantic. This suggests that plume material flowing outward from Iceland is not confined to a rheological groove formed by thin lithosphere along the ridge axis but instead flows outward from Iceland over a broad area.

normal seafloor spreading. The transition from V_{SH} fast to V_{SV} fast coincides with the appearance of increased hot spot–ridge interaction approximately 20 Myr ago, suggesting that the anomalous $V_{SV} > V_{SH}$ region is a direct result of the hot spot influence.

7. Discussion

[36] Our study indicates that a significant part of the upper mantle in the North Atlantic is affected by the Icelandic hot spot (Figure 10). The sublithospheric low-velocity zone and its corresponding $\sim 50^\circ$ – 75° thermal anomaly fill at least half of the distance between the continental shelf of Greenland and the Rockall Plateau, a continental block to the northwest of Ireland. Our results show that plume material from beneath Iceland is not confined to a rheological groove formed by the cooling of the lithosphere. Anomalous slow material is seen in the upper mantle beneath lithosphere to depths of 100–150 km and out to ~ 35 Ma. If the shallow lithospheric groove at the ridge axis is filled with high-viscosity material because of the dehydration of the mantle upon partial melting (as suggested by Hirth and Kohlstedt [1996] and Ito *et al.* [1999]), then upwelling material is expected to spread out broadly below this high-viscosity region [Ito *et al.*, 1999; Ito, 2001]. However, we suggest that the layer of plume material is voluminous enough to spread out broadly without this requirement. Given that the Icelandic hot spot has been coincident with the North Atlantic Ocean for at least 40 Ma [Lawver and Muller, 1994] and coincident with the Reykjanes Ridge for the last 16 Ma [White, 1997], a great deal of plume material may now be present in the asthenosphere in the North Atlantic.

[37] Gaherty [2001] and Braun *et al.* [2000] suggested that observations of $V_{SV} > V_{SH}$ in the asthenosphere and lithosphere may be caused by buoyant upwelling. Our observation of a strong $V_{SV} > V_{SH}$ pattern beneath the Eurasian plate is consistent with a buoyancy effect com-

bined with a nearly stationary plate and little horizontal shear (Figure 11a). Note that in the spreading direction (i.e., $\sim 28^\circ$ oblique from normal to the ridge axis), the Eurasian plate is moving 6 mm/yr westward with respect to a hot spot reference frame [Gripp and Gordon, 2002] (Figure 1). On the other hand, where the pattern is weak beneath the North American plate, which is moving westward at 25 mm/yr, any buoyancy effect may become overprinted by the larger horizontal shear that may occur there. The strength of the $V_{SV} > V_{SH}$ pattern near the Reykjanes ridge appears to be unique as compared to other asymmetrically spreading regions, including the Kolbeinsey ridge and the MAR south of the equator [Gaherty and Dunn, 2007]. Perhaps anomalously high temperatures beneath the Reykjanes region induce rare buoyancy-driven flow, yet it is not clear that

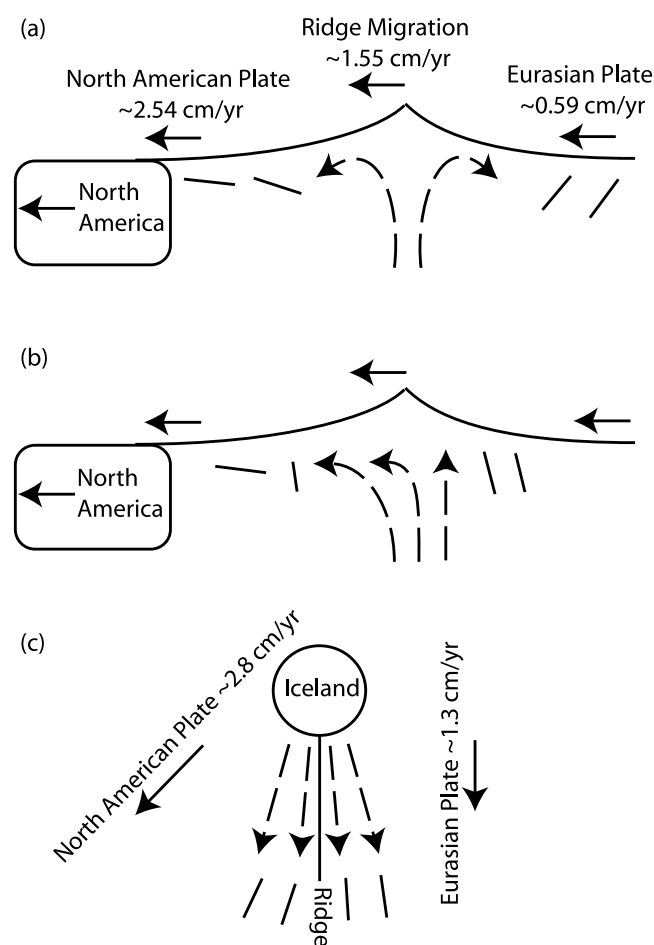


Figure 11. Three possible mantle flow scenarios to explain the existence of our anomalous anisotropy structure. Solid lines with arrows indicate plate motion direction, dashed lines with arrows indicate mantle flow directions, and solid lines without arrows indicate crystallographic [100] alignment. Spreading rates listed on the plots are the rates projected into the relative spreading direction. (a) Buoyant upwelling beneath the ridge as suggested by Gaherty [2001]. (b) Asymmetric corner flow. (c) Strong southward plume flow (map view). Each of these scenarios, or a combination of them, may be consistent with the observed anisotropy patterns.

buoyancy-enhanced upwelling is required to explain the anisotropy pattern.

[38] Mantle flow models of strongly asymmetric, passive spreading provide strain field estimates that suggest that vertical fabric may be retained beneath the nearly stationary plate even in the absence of buoyancy forces [Blackman and Kendall, 2002]. In this scenario (Figure 11b), olivine fast axes develop a vertical alignment during upwelling beneath the ridge, and then this fabric is preserved beneath the Eurasian plate where horizontal shear is small. The weaker $V_{SV} > V_{SH}$ anisotropy beneath the North American plate may then reflect a stronger component of horizontal shear induced by the overriding plate, such that the crystallographic axes are realigning into the horizontal plane at a much faster rate on this side of the ridge. One possible problem with this interpretation is that it is not clear why the vertical fabric retained off axis would be stronger than that directly beneath the axis unless vertical shear continues off axis and the strength of the fabric continues to grow. In addition, there appears to be a good correlation between the appearance of lithosphere with $V_{SV} > V_{SH}$ and the initiation of hot spot–influenced spreading at 20 Ma. There was no significant change in plate motion 20 Myr ago. Finally, as noted above, the $V_{SV} > V_{SH}$ pattern is not observed along other regions of the MAR where seismic studies have been done [Gaherty and Dunn, 2007].

[39] A third explanation is that strong southward shear due to plume flow beneath the plate aligns the fast axes of anisotropic minerals in the ridge parallel direction (Figure 11c). From the orientation of the V-shaped ridges, ridge-parallel plume flow is predicted to be 10 times faster than the half seafloor spreading rate [White et al., 1995]. This could produce a relatively weak form of $V_{SV} > V_{SH}$ anisotropy [Maupin, 1985], which could be enhanced if the flow plane of the deformation is vertical (or nearly so) by one of two mechanisms: vertical alignment of the olivine fabric perpendicular to the flow direction due to deformation under melt-rich conditions [Holtzman et al., 2003], or formation of a strong orthorhombic fabric with a ridge-parallel fast direction and a horizontal, ridge-perpendicular slow axis. Yet the reliance of a nearly vertical flow plane or shear wall along axis invokes images of channelized flow, of which we see no evidence in our mean velocity images.

[40] Our results and the gravity data indicate that the thickness of the lithosphere is asymmetric across the ridge, with the North American plate much thinner than the Eurasian plate (Figure 7a), suggesting that the North American plate cools more slowly. Yale and Phipps Morgan [1998] suggest that mantle flow in the asthenosphere of the North Atlantic is preferentially directed toward the west because of the recession of the North American continental margin. As the continental root migrates westward, a zone of negative pressure develops behind the root in the upper mantle drawing in material from adjacent regions, perhaps including hotter plume material. To the east, the Eurasian plate does not appreciably recess from the Reykjanes Ridge and so there is no such effect. A second explanation may be that relatively higher shear beneath the North American plate produces greater shear heating and thus a thinner lithosphere. A third possibility is that hot plume material accumulated beneath the North American plate in earlier

times, when the plume was located west of the Mid-Atlantic Ridge.

8. Conclusions

[41] 1. In the North Atlantic south of Iceland, we observe a broad (500–600 km) and deep (to 100–150 km depth) anomalously low-velocity region beneath the lithospheric lid. The velocity anomaly is consistent with a ~ 75 degree excess temperature, which we suggest is the result of Icelandic plume material spreading out broadly to the south.

[42] 2. Anomalous $V_{SV} > V_{SH}$ anisotropy is observed in an asymmetric pattern beneath the Reykjanes Ridge out to roughly 20 Ma, which is the time of initiation of hot spot–influenced spreading. A variety of mechanisms may produce this anisotropy pattern, including ridge-parallel plume flow and buoyant upwelling.

[43] **Acknowledgments.** All maps are produced using GMT software [Wessel and Smith, 1998]. Bathymetry data in Figure 1 are from the ETOPO5 data set (<http://www.ngdc.noaa.gov/mgg/global/global.html>). Data from station BORG are courtesy of the Global Seismograph Network [Butler et al., 2004]. All HOTSPOT and ICEMELT data and instrument responses come courtesy of IRIS (<http://www.iris.edu>) [Aster et al., 2005]. Earthquake source parameters are from the International Seismological Centre *Online Bulletin*, available at <http://www.isc.ac.uk>, the Engdahl catalog [Engdahl et al., 1998], and the Global CMT Project available at <http://www.globalcmt.org> [e.g., Ekström et al., 2005]. Initial data processing was performed using the software package SAC [Goldstein, 1996]. We thank Donna Blackman and an anonymous referee for their thoughtful reviews of the manuscript. This research was supported by NSF grant OCE03-37237 (RAD) and OCE04-36398 (J.B.G.).

References

- Aki, K., and P. G. Richards (2002), *Quantitative Seismology*, Univ. Sci. Books, Sausalito, Calif.
- Albers, M., and U. R. Christensen (2001), Channeling of plume flow beneath mid-ocean ridges, *Earth Planet. Sci. Lett.*, **187**, 207–220.
- Allen, R. M., et al. (1999), The thin hot plume beneath Iceland, *Geophys. J. Int.*, **137**, 51–63.
- Allen, R. M., et al. (2002), Imaging the mantle beneath Iceland using integrated seismological techniques, *J. Geophys. Res.*, **107**(B12), 2325, doi:10.1029/2001JB000595.
- Aster, R., J. Beaudoin, J. Hole, M. Fouch, J. Fowler, and D. James (2005), IRIS Seismology Program marks 20 years of discovery, *Eos Trans. AGU*, **86**, 171.
- Babuska, V., and M. Cara (1991), *Seismic Anisotropy in the Earth, Mod. Approaches Geophys.*, vol. 10, Kluwer Acad., Dordrecht, Netherlands.
- Backus, G. E. (1965), Possible forms of seismic anisotropy of the uppermost mantle under oceans, *J. Geophys. Res.*, **70**, 3429–3439.
- Ben Ismail, W., and D. Mainprice (1998), An olivine fabric database: An overview of upper mantle fabrics and seismic anisotropy, *Tectonophysics*, **296**, 145–157.
- Bijwaard, H., and W. Spakman (1998), Closing the gap between regional and global travel time tomography, *J. Geophys. Res.*, **103**, 30,055–30,078.
- Bijwaard, H., and W. Spakman (1999), Tomographic evidence for a narrow whole mantle plume below Iceland, *Earth Planet. Sci. Lett.*, **166**, 121–126.
- Bjarnason, I. T., C. J. Wolfe, S. C. Solomon, and G. B. Gudmundsson (1996), Initial results from the ICEMELT experiment: Body-wave delay times and shear-wave splitting across Iceland, *Geophys. Res. Lett.*, **23**, 459–462.
- Blackman, D. K., and J.-M. Kendall (2002), Seismic anisotropy in the upper mantle 2. Predictions for current plate boundary flow models, *Geochem. Geophys. Geosyst.*, **3**(9), 8602, doi:10.1029/2001GC000247.
- Braun, M. G., G. Hirth, and E. M. Parmentier (2000), The effects of deep damp melting on mantle flow and melt generation beneath mid-ocean ridges, *Earth Planet. Sci. Lett.*, **176**, 339–356.
- Butler, R., et al. (2004), The Global Seismographic Network surpasses its design goal, *Eos Trans. AGU*, **85**, 225.
- Darbyshire, F. A., I. T. Bjarnason, R. S. White, and O. G. Flovenz (1998), Crustal structure above the Iceland mantle plume imaged by the ICEMELT refraction profile, *Geophys. J. Int.*, **135**, 1131–1149.

- Dater, D., D. Metzger, and A. Hittelman (1999), *Land and Marine Gravity* [CD-ROM], Natl. Geophys. Data Cent., NOAA, Boulder, Colo.
- DeMets, C., R. G. Gordon, D. F. Argus, and S. Stein (1994), Effect of recent revisions to the geomagnetic reversal time scale on estimates of current plate motions, *Geophys. Res. Lett.*, **21**, 2191–2194.
- Dunn, R. A., and D. W. Forsyth (2003), Imaging the transition between the region of mantle melt generation and the crustal magma chamber beneath the southern East Pacific Rise with short-period Love waves, *J. Geophys. Res.*, **108**(B7), 2352, doi:10.1029/2002JB002217.
- Dunn, R. A., D. R. Toomey, and S. C. Solomon (2000), Three-dimensional seismic structure and physical properties of the crust and shallow mantle beneath the East Pacific Rise at 9°30'N, *J. Geophys. Res.*, **105**, 23,537–23,555.
- Einarsson, P. B. B., M. T. Gudmundsson, H. Björnsson, K. Grinvald, and F. Sigmundsson (1997), Center of the Iceland hotspot experiences volcanic unrest, *Eos Trans. AGU*, **78**, 369.
- Ekström, G., A. M. Dziewonski, N. N. Maternovskaya, and M. Nettles (2005), Global seismicity of 2003: Centroid-moment-tensor solutions for 1087 earthquakes, *Phys. Earth Planet. Inter.*, **148**(2–4), 327–351.
- Engdahl, E. R., R. D. Van der Hilst, and R. P. Buland (1998), Global teleseismic earthquake relocation with improved travel times and procedures for depth determination, *Bull. Seismol. Soc. Am.*, **88**, 722–743.
- Faul, U. H., and I. Jackson (2005), The seismological signature of temperature and grain size variation in the upper mantle, *Earth Planet. Sci. Lett.*, **234**, 119–134.
- Fitton, J. G., A. D. Saunders, M. J. Norry, B. S. Hardarson, and R. N. Taylor (1997), Thermal and chemical structure of the Iceland plume, *Earth Planet. Sci. Lett.*, **153**, 197–208.
- Foulger, G. R., and D. G. Pearson (2001), Is Iceland underlain by a plume in the lower mantle? Seismology and helium isotopes, *Geophys. J. Int.*, **145**, F1–F5.
- Foulger, G. R., et al. (2000), The seismic anomaly beneath Iceland extends down to the mantle transition zone and no deeper, *Geophys. J. Int.*, **142**, F1–F5.
- Gaherty, J. (2001), Seismic evidence for hotspot-induced buoyant flow beneath the Reykjanes Ridge, *Science*, **293**, 1645–1647.
- Gaherty, J. B., and R. A. Dunn (2007), Evaluating hot spot–ridge interaction in the Atlantic from regional-scale seismic observations, *Geochem. Geophys. Geosyst.*, **8**, Q05006, doi:10.1029/2006GC001533.
- Goldstein, P. (1996), SAC2000: Seismic signal processing and analysis tools for the 21st century, *Seismol. Res. Lett.*, **67**, 39.
- Gripp, A. E., and R. G. Gordon (2002), Young tracks of hotspots and current plate velocities, *Geophys. J. Int.*, **150**, 321–361.
- Gu, Y. J., S. C. Webb, A. Lerner-Lam, and J. B. Gaherty (2005), Upper mantle structure beneath the eastern Pacific Ocean ridges, *J. Geophys. Res.*, **110**, B06305, doi:10.1029/2004JB003381.
- Hammond, W. C., and E. D. Humphreys (2000), Upper mantle seismic wave velocity: Effects of realistic partial melt geometries, *J. Geophys. Res.*, **105**, 10,975–10,986.
- Hammond, W. C., and D. R. Toomey (2003), Seismic velocity anisotropy and heterogeneity beneath the Mantle Electromagnetic and Tomography Experiment (MELT) region of the East Pacific Rise from analysis of *P* and *S* body waves, *J. Geophys. Res.*, **108**(B4), 2176, doi:10.1029/2002JB001789.
- Hardarson, B. S., J. G. Fitton, R. M. Ellam, and M. S. Pringle (1997), Rift relocation: A geochemical and geochronological investigation of a paleorift in northwest Iceland, *Earth Planet. Sci. Lett.*, **153**, 181–196.
- Heller, D.-A., and G. Marquart (2002), An admittance study of the Reykjanes Ridge and elevated plateau between the Charlie-Gibbs and Senja fracture zones, *Geophys. J. Int.*, **148**, 65–76.
- Hess, H. H. (1964), Seismic anisotropy of the uppermost mantle under oceans, *Nature*, **203**, 629–630.
- Hirth, G., and D. L. Kohlstedt (1996), Water in the oceanic upper mantle: Implications for rheology, melt extraction and the evolution of the lithosphere, *Earth Planet. Sci. Lett.*, **144**, 93–108.
- Holtzman, B. K., D. L. Kohlstedt, M. E. Zimmerman, F. Heidelbach, T. Hiraga, and J. Hustoft (2003), Melt segregation and strain partitioning: Implications for seismic anisotropy and mantle flow, *Science*, **301**, 1227–1230.
- Ito, G. (2001), Reykjanes 'V'-shaped ridges originating from a pulsing and dehydrating mantle plume, *Nature*, **411**, 681–684.
- Ito, G., J. Lin, and C. W. Gable (1996), Dynamics of mantle flow and melting at a ridge centered hotspot: Iceland and the Mid-Atlantic Ridge, *Earth Planet. Sci. Lett.*, **144**, 53–74.
- Ito, G., Y. Shen, G. Hirth, and C. J. Wolfe (1999), Mantle flow, melting, and dehydration of the Iceland mantle plume, *Earth Planet. Sci. Lett.*, **165**, 81–96.
- Ito, G., J. Lin, and D. Graham (2003), Observational and theoretical studies of the dynamics of mantle plume–mid-ocean ridge interaction, *Rev. Geophys.*, **41**(4), 1017, doi:10.1029/2002RG000117.
- Jones, S. M., N. White, and J. MacLennan (2002), V-shaped ridges around Iceland: Implications for spatial and temporal patterns of mantle convection, *Geochem. Geophys. Geosyst.*, **3**(10), 1059, doi:10.1029/2002GC000361.
- Jordan, T. H. (1979), Mineralogies, densities and seismic velocities of garnet hercynites and their geophysical implications, in *The Mantle Sample: Inclusions in Kimberlites and Other Volcanics (Proceedings of the Second International Kimberlite Conference)*, vol. 2, pp. 1–14, AGU, Washington, D. C.
- Kaminski, E., and N. M. Ribe (2002), Timescales for the evolution of seismic anisotropy in mantle flow, *Geochem. Geophys. Geosyst.*, **3**(8), 1051, doi:10.1029/2001GC000222.
- Kawasaki, I., and F. Kon'no (1984), Azimuthal anisotropy of surface-waves and the possible type of the seismic anisotropy due to preferred orientation of olivine in the uppermost mantle beneath the Pacific Ocean, *J. Phys. Earth*, **32**(3), 229–244.
- Keeton, J. A., R. C. Searle, B. Parsons, R. S. White, B. J. Murton, L. M. Parson, C. Peirce, and M. C. Sinha (1997), Bathymetry of the Reykjanes Ridge, *Mar. Geophys. Res.*, **19**, 55–64.
- Lawver, L. A., and R. D. Muller (1994), Iceland hotspot track, *Geology*, **22**, 311–314.
- Li, A., and R. S. Detrick (2003), Azimuthal anisotropy and phase velocity beneath Iceland: Implication for plume-ridge interaction, *Earth Planet. Sci. Lett.*, **206**, 1–13, doi:10.1016/S0012-821X(03)00382-0.
- Maupin, V. (1985), Partial derivatives of surface wave phase velocities for flat anisotropic models, *Geophys. J. R. Astron. Soc.*, **83**, 379–398.
- Montelli, R., G. Nolet, F. A. Dahlen, G. Masters, E. R. Engdahl, and S.-H. Hung (2004), Finite-frequency tomography reveals a variety of plumes in the mantle, *Science*, **303**, 338–343, doi:10.1126/science.1092485.
- Morgan, W. J. (1971), Convection plumes in the lower mantle, *Nature*, **230**, 42–43.
- Morgan, W. J. (1981), Hotspot tracks and the opening of the Atlantic and Indian oceans, *The Sea*, pp. 443–487, Wiley Interscience, New York.
- Murton, B. J., R. N. Taylor, and M. F. Thirwall (2002), Plume-ridge interaction: A geochemical perspective from the Reykjanes Ridge, *J. Petrol.*, **43**, 1987–2012.
- Nataf, H.-C. (2000), Seismic imaging of mantle plumes, *Annu. Rev. Earth Planet. Sci.*, **28**, 391–417.
- National Geophysical Data Center (1993), 5-Minute Gridded Global Relief Data on CD-ROM (ETOPO5), Data Announcement 93-MGG-01, <http://www.ngdc.noaa.gov>, Boulder, Colo.
- National Geophysical Data Center (2005), Total Sediment Thickness of the World's Oceans and Marginal Seas, <http://www.ngdc.noaa.gov>, Boulder, Colo.
- Nishimura, C. E., and D. W. Forsyth (1988), The anisotropic structure of the upper mantle in the Pacific, *Geophys. J.*, **96**, 203–209.
- Nolet, G. (1987), Seismic wave propagation and seismic tomography, in *Seismic Tomography With Applications in Global Seismology and Exploration Geophysics*, edited by G. Nolet, pp. 1–23, D. Reidel, Dordrecht, Netherlands.
- Paige, C. C., and M. A. Saunders (1982), LSQR: An algorithm for sparse linear equations and sparse least squares, *ACM Trans. Math. Software*, **8**, 43–71.
- Piliidou, S., K. Priestley, O. Gudmundsson, and E. Debayle (2004), Upper mantle S-wave speed heterogeneity and anisotropy beneath the North Atlantic from regional surface wave tomography: The Iceland and Azores plumes, *Geophys. J. Int.*, **159**, 1057–1076, doi:10.1111/j.1365-246X.2004.02462.x.
- Poreda, R., J. G. Schilling, and H. Craig (1986), Helium and hydrogen isotopes in ocean-ridge basalts north and south of Iceland, *Earth Planet. Sci. Lett.*, **78**, 1–17.
- Ribe, N. M., U. R. Christensen, and J. Theibing (1995), The dynamics of plume-ridge interaction, 1: Ridge-centered plumes, *Earth Planet. Sci. Lett.*, **134**, 155–168.
- Ritsema, J., H. J. Van Heijst, and J. H. Woodhouse (1999), Complex shear wave velocity structure imaged beneath Africa and Iceland, *Science*, **286**, 1925–1928.
- Schilling, J. G. (1973), Iceland mantle plume: Geochemical study of Reykjanes Ridge, *Nature*, **242**, 565–571.
- Schilling, J. G. (1985), Upper mantle heterogeneities and dynamics, *Nature*, **314**, 62–67.
- Schmelling, H., G. Marquart, and T. Ruedas (2003), Pressure- and temperature-dependent thermal expansivity and the effect on mantle convection and surface observables, *Geophys. J. Int.*, **154**, 224–229.
- Searle, R. C., J. A. Keeton, R. B. Owens, R. S. White, R. Mecklenburgh, B. Parsons, and S. M. Lee (1998), The Reykjanes Ridge: Structure and tectonics of a hot-spot-influenced, slow-spreading ridge, from multibeam bathymetry, gravity, and magnetic investigations, *Earth Planet. Sci. Lett.*, **160**, 463–478.

- Smallwood, J. R., R. S. White, and T. A. Minshull (1995), Sea-floor spreading in the presence of the Iceland plume: The structure of the Reykjanes Ridge at 61°40'N, *J. Geol. Soc. London*, **152**, 1023–1029.
- Takeuchi, H., and M. Saito (1972), Seismic surface waves, *Methods Comput. Phys.*, **11**, 217–295.
- Talwani, M. (1971), Reykjanes ridge crest: A detailed geophysical study, *J. Geophys. Res.*, **76**, 473–517.
- Talwani, M., J. L. Worzel, and M. Landisman (1959), Rapid gravity computations for two-dimensional bodies with application to the Mendocino submarine fracture zone, *J. Geophys. Res.*, **64**, 49–59.
- Tarantola, A. (1987), *Inverse Problem Theory*, Elsevier, Amsterdam.
- Taylor, R. N., M. F. Thirwall, B. J. Murton, D. R. Hilton, and M. A. M. Gee (1997), Isotopic constraints on the influence of the Icelandic plume, *Earth Planet. Sci. Lett.*, **148**, E1–E8.
- Toomey, D. R., W. S. D. Wilcock, S. C. Solomon, W. C. Hammond, and J. A. Orcutt (1998), Mantle seismic structure beneath the MELT region of the East Pacific Rise from P and S wave tomography, *Science*, **280**, 1224–1227.
- Turcotte, D. L., and G. Schubert (2002), *Geodynamics*, Cambridge Univ. Press, Cambridge, U. K.
- van der Lee, S. (2002), High-resolution estimates of lithospheric thickness from Missouri to Massachusetts, USA, *Earth Planet. Sci. Lett.*, **203**, 15–23.
- Vogt, P. R. (1971), Asthenosphere motion recorded by the ocean floor south of Iceland, *Earth Planet. Sci. Lett.*, **13**, 153–160.
- Vogt, P. R. (1976), Plume, subaxial pipe flow, and topography along the mid-ocean ridges, *Earth Planet. Sci. Lett.*, **29**, 309–325.
- Wessel, P., and W. H. F. Smith (1998), New, improved version of the Generic Mapping Tools released, *Eos Trans. AGU*, **79**, 579.
- White, R. S. (1997), Rift-plume interaction in the North Atlantic, *Philos. Trans. R. Soc. London*, **355**, 319–339.
- White, R. S., and D. McKenzie (1989), Magmatism at rift zones: The generation of volcanic continental margins and flood basalts, *J. Geophys. Res.*, **95**, 7685–7729.
- White, R. S., J. W. Brown, and J. R. Smallwood (1995), The temperature of the Iceland plume and origin of outward propagating V-shaped ridges, *J. Geol. Soc. London*, **152**, 1039–1045.
- Whitmarsh, R. B., and A. J. Calvert (1986), Crustal structure of the Atlantic fracture zones—I. The Charlie-Gibbs Fracture Zone, *Geophys. J. R. Astron. Soc.*, **108**, 16–34.
- Wolfe, C. J., I. T. Bjarnason, J. C. VanDecar, and S. C. Solomon (1997), Seismic structure of the Iceland mantle plume, *Nature*, **385**, 245–247.
- Xue, M., and R. M. Allen (2005), Asthenospheric channeling of the Icelandic upwelling: Evidence from seismic anisotropy, *Earth Planet. Sci. Lett.*, **235**, 167–182, doi:10.1016/j.epsl.2005.03.017.
- Yale, M. M., and J. Phipps Morgan (1998), Asthenosphere flow model of hotspot-ridge interactions: A comparison of Iceland and Kerguelen, *Earth Planet. Sci. Lett.*, **161**, 45–56.
- Yang, Y. Y., D. W. Forsyth, and D. S. Weeraratne (2007), Seismic attenuation near the East Pacific Rise and the origin of the low-velocity zone, *Earth Planet. Sci. Lett.*, **258**, 260–268, doi:10.1016/j.epsl.2007.03.040.
- Yomogida, K., and K. Aki (1985), Waveform synthesis of surface waves in a laterally heterogeneous Earth by the Gaussian beam method, *J. Geophys. Res.*, **90**, 7665–7688.
- Zhang, S., S. I. Karato, J. F. Gerald, U. H. Faul, and Y. Zhou (2000), Simple shear deformation of olivine aggregates, *Tectonophysics*, **316**, 133–152.
- Zhao, D. (2004), Global tomographic images of mantle plumes and subducting slabs: Insight into deep Earth dynamics, *Phys. Earth Planet. Inter.*, **146**, 3–34, doi:10.1016/j.pepi.2003.07.032.

A. A. Delorey, Earth and Space Sciences, University of Washington, 4000 15th Avenue NE, Seattle, WA 98195-1310, USA. (adelorey@u.washington.edu)

R. A. Dunn, Department of Geology and Geophysics, SOEST, University of Hawaii, 1680 East-West Road, Honolulu, HI 96822, USA. (dunnr@hawaii.edu)

J. B. Gaherty, Lamont-Doherty Earth Observatory of Columbia University, PO Box 1000, Palisades, NY 10964-8000, USA. (gaherty@ldeo.columbia.edu)